

# Internal gravity waves generated by a turbulent bottom Ekman layer

JOHN R. TAYLOR AND SUTANU SARKAR

Mechanical and Aerospace Engineering, University of California, San Diego, La Jolla, CA 92093, USA

(Received 6 November 2006 and in revised form 21 June 2007)

Internal gravity waves excited by the turbulent motions in a bottom Ekman layer are examined using large-eddy simulation. The outer flow is steady and uniformly stratified while the density gradient is set to zero at the flat lower wall. After initializing with a linear density profile, a mixed layer forms near the wall separated from the ambient stratification by a pycnocline. Two types of internal wave are observed. Waves with frequencies larger than the free-stream buoyancy frequency are seen in the pycnocline, and vertically propagating internal waves are observed in the outer layer with characteristic frequency and wavenumber spectra. Since a signature of the pycnocline waves is observed in the frequency spectrum of the mixed layer, these waves may affect the boundary-layer turbulence. The dominant outer-layer waves have a group velocity directed  $35 - 60^\circ$  from the vertical axis, which is consistent with previous laboratory studies. The energy flux associated with the radiated waves is small compared to the integrated dissipation in the boundary layer, but is of the same order as the integrated buoyancy flux. A linear model is proposed to estimate the decay in wave amplitude owing to viscous effects. Starting from the observed wave amplitudes at the bottom of the pycnocline, the model prediction for the spectral distribution of the outer layer wave amplitude compares favourably with the simulation results.

---

## 1. Introduction

When turbulence is present in a stably stratified fluid, internal gravity waves are often created and radiate energy away from the source region. Turbulence-generated internal waves have been observed in a variety of flows: wakes (Bonneton, Chomaz & Hopfinger 1993; Gourlay *et al.* 2001; Spedding 2002; Diamessis, Domaradzki & Hesthaven 2005), shear layers (Sutherland & Linden 1998; Sutherland, Caulfield & Peltier 1994; Basak & Sarkar 2006), in the lee of topography (Aguilar & Sutherland 2006), grid-generated turbulence (Linden 1975; E & Hopfinger 1986; Dohan & Sutherland 2003, 2005) and gravity currents (Flynn & Sutherland 2004). The turbulence that generates the internal waves may be associated with an essentially well-mixed region (e.g. grid turbulence) or a stratified region (e.g. wakes and shear layers). This study will be focused on an example of the former case. Turbulence-generated internal waves may be important to the flow evolution since they are capable of extracting energy and momentum from a forced region, propagating to another nearby or remote location, and depositing their energy and momentum through a variety of possible mechanisms (e.g. wave breaking, wave/wave interactions, critical-layer absorption).

In the ocean and in the atmosphere, one important site of intense turbulence is near boundaries. The problem of a turbulent region driven by internal waves incident on

a boundary has been considered in several studies (e.g. Slinn & Riley 1998; Thorpe 2001; D'Asaro 1982), but it appears that the problem of internal waves generated by boundary-layer turbulence has not been investigated. Since boundary regions are a hotspot of kinetic energy dissipation (Gregg *et al.* 1999; Garrett & St Laurent 2002), if the waves are able to extract even a fraction of the kinetic energy from near the boundary and transfer it to a less energetic region, they may play an important role in the global energy budget.

There is some evidence suggestive of turbulence-generated internal waves in the observations of Moum *et al.* (1992) from the upper equatorial ocean. A weakly stratified turbulent surface layer was diurnally forced by a combination of a wind stress and surface heat flux. Large-amplitude internal waves were observed in the thermocline with a narrow range of wavenumbers. These waves were observed during times of strong wind and unstable convective forcing, suggesting that they may have been forced by turbulent motions near the sea surface. In addition, the turbulent dissipation rate in the thermocline was found to be correlated to the level of internal wave activity.

There is evidence that internal gravity waves are important to atmospheric dynamics (see Fritts & Alexander 2003 for a review). Gravity waves affect the large-scale dynamics in the mesosphere and stratosphere through the so-called 'wave-drag' exerted on the mean flow (Holton & Alexander 2000). Sources of turbulence-generated internal waves in the atmosphere include convective motions and shear instabilities (Fritts & Alexander 2003). Buhler, McIntyre & Scinocca (1999) and Buhler & McIntyre (1999) considered the generation of internal waves by a localized unstable shear layer at the top of the jet stream. They used ray tracing to estimate the transmission of waves into the mesosphere and concluded that these waves may be an important source term in the local momentum budget.

The importance of turbulence-generated internal waves to the growth of a mixed region was considered by Linden (1975). An oscillating grid was used to generate a turbulent mixed layer above a density-stratified region. As the mixed layer deepened, a pycnocline developed with a density gradient up to three times the value in the outer region. Internal waves were observed propagating away from the mixed region when the outer layer had a linear stratification instead of being homogeneous. The relative importance of the internal waves was quantified by comparing the rate of change of potential energy to the internal wave energy flux, and it was found that the presence of propagating internal waves may reduce the mixed-layer growth by up to 50%. A different conclusion was reached by E & Hopfinger (1986) who also considered shear-free grid-generated turbulence. With two initial conditions, a uniformly stratified fluid and a two-layer system, they found that the rate of mixed-layer growth depends on the density jump at the interface, but not on the density structure away from the mixed region. Based on this observation, and an estimate of the internal wave energy flux relative to the turbulence flux, they concluded that radiated internal waves, which exist only in the continuously stratified case, do not significantly affect the growth of the mixed layer.

As a mixed region forms in a stratified fluid, it is common for a region of strong density gradient, or pycnocline, to form at the edge of the mixed layer. Since the density gradient in the pycnocline forms a local maximum, it is possible for high-frequency waves to become isolated in this layer. Piat & Hopfinger (1981) considered a turbulent boundary layer in a fluid with a two-layer thermal structure. They found that the mean shear and root mean square velocity increased at the thermal interface. Internal waves travelling along the interface had a time-lag correlation between

vertical velocity and temperature fluctuation that was  $90^\circ$  out of phase. The authors reported that the waves occurred in bursts generated by the interactions of turbulent eddies with the interface. The frequency of the observed waves was approximately equal to the buoyancy frequency at the interface.

Since the turbulent region that provides energy to the wave field is composed of many spatial and temporal scales, it is perhaps surprising that the vertically propagating turbulence-generated internal waves are often associated with a relatively narrow frequency range that is proportional to the local buoyancy frequency. The angle made by the group velocity vector and the vertical direction is set from the dispersion relation, which for non-rotating linear internal gravity waves is  $\omega = N \cos \Theta$ , where  $\omega$  is the intrinsic frequency,  $N$  is the background buoyancy (or Brunt–Väisälä) frequency, and  $\Theta$  is the angle between the wavenumber vector and the horizontal axis. Therefore, waves with a particular frequency are also associated with a characteristic angle of propagation. Previous studies of turbulence-generated internal waves have generally found that  $35^\circ < \Theta < 60^\circ$ . Several explanations have been given for this frequency selection as discussed below.

Sutherland & Linden (1998) conducted a laboratory experiment with stratified fluid flowing over a vertical barrier. A turbulent shear layer formed in the wake of the barrier and internal waves were observed propagating away from the shear layer through the uniformly stratified surrounding fluid. The largest-amplitude waves were associated with an angle of propagation in the range  $45^\circ < \Theta < 60^\circ$ . The authors noted that the vertical component of the group velocity is maximum for waves with  $\Theta = 45^\circ$  (for a fixed wavelength) and suggested that if turbulence in the mixed region had a uniform frequency distribution, waves with this angle may optimally transport energy away from the mixed region. They also suggested that the radiated internal waves with  $\Theta = 45^\circ$  may modify the mean flow so as to favour generation of waves with their own frequency.

An alternative hypothesis for the narrow frequency range observed in laboratory experiments was proposed by Sutherland (2001). He derived stability criteria for internal waves for two types of instability. For low-frequency waves, convective overturning provides the most stringent stability criteria based on the wave amplitude. For high-frequency waves the lowest critical wave amplitude is based on resonant interactions between the wave and its wave-induced mean flow, a process that steepens the waves until they become statically unstable. Based on the predicted stability criteria for these two mechanisms, it was shown that the largest critical amplitude corresponds to waves propagating at  $\Theta = 45^\circ$ . Sutherland (2001) hypothesized that since other angles would become unstable at a lower amplitude, these instability mechanisms may explain the frequency selection observed in laboratory experiments.

Dohan & Sutherland (2003) described laboratory experiments using an oscillating grid to create a turbulent mixed region in a uniformly stratified tank. A novel visualization technique was used in order to examine the internal waves in detail. The background buoyancy frequency was varied by over a factor of 4 and in all cases, the frequency of the waves was such that the vertical angle of propagation was in the range  $42^\circ < \Theta < 55^\circ$ . The authors explored two explanations for the narrow range of observed propagation angles. The first was that waves at frequencies other than those observed would become unstable through the mechanisms proposed by Sutherland (2001). Since the amplitudes of the waves were only about 25% of that predicted for instability, this explanation was deemed unlikely. They concluded that a better explanation was a resonant feedback between the waves and turbulence. Since waves at  $35^\circ$  have a maximum vertical energy flux and waves at  $45^\circ$  have a maximum

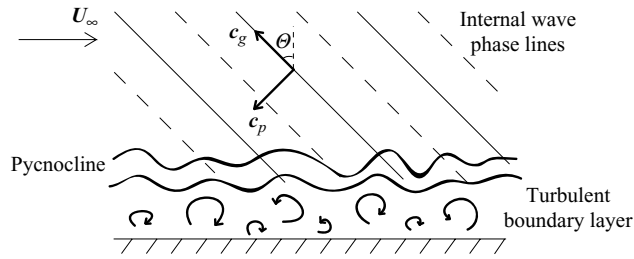


FIGURE 1. Internal wave excitation from a turbulent boundary layer. The group and phase velocity are shown relative to the free stream.

momentum flux, they speculated that waves near these frequencies may extract energy from the turbulent region in an optimal way. Dohan & Sutherland (2005) compared a two-dimensional numerical simulation to laboratory experiments similar to their previous study. Turbulence in the simulations was generated by a small-scale forcing term with a randomized Gaussian spectrum in the horizontal and vertical directions, in addition to a large-scale counter-rotating vortex pair. The characteristic length scale of the turbulence-generated internal waves was between those associated with the large- and small-scale forcing. The range of  $\Theta$  in the simulations was similar to that observed in the laboratory experiments.

Keeler, Bondur & Gibson (2005) reported surface manifestations of internal waves generated by turbulent motions above a submerged municipal wastewater outfall. Based on observations from previous laboratory experiments, the authors hypothesized that the internal waves propagated upwards with  $\Theta \approx 45^\circ$ . Gibson *et al.* (2006) proposed an explanation for the selection of high-frequency waves. First, energy is transferred from turbulent motions to internal waves through fossilization at the buoyancy frequency. These waves do not propagate vertically since the vertical component of the group velocity for waves at  $\omega = N$  vanishes. Inertial-vortex forces were then invoked to explain a reduction in the frequency of the waves which are then able to propagate vertically. The length scale associated with these waves was predicted to be proportional to the Ozmidov scale at the time of fossilization.

The present study is based on simulations of a bottom Ekman layer with a uniform density stratification outside the boundary layer (figure 1). The focus of this paper will be on the internal waves excited by turbulent motions in the bottom boundary layer. While previous laboratory and two-dimensional numerical studies have considered the generation of internal waves from a well-mixed turbulent region, this has not yet been examined in the case of boundary layers. The three-dimensional structure of the waves will be examined, and compared with the general characteristics of turbulence-generated internal waves previously observed in laboratory experiments. An attempt to explain the amplitude and frequency of the radiated waves in our simulations will be offered. The importance of the radiated internal waves to the dynamics of the boundary layer will also be addressed by comparing the internal wave energy flux to the integrated turbulent dissipation rate and the integrated buoyancy flux.

## 2. Formulation

The turbulent boundary layer that is considered here is generated when a steady flow in geostrophic balance encounters a smooth flat wall. Near the wall, where the turbulent viscosity contributes to the leading-order momentum balance, the flow

Simulation	$Ri_*$	$N_\infty/f$	$Re_*$	$Pr$
1	0	0	960	
1 <sub>h</sub>	0	0	1920	
2	100	10	960	5
2 <sub>h</sub>	100	10	1920	
3	1000	31.6	960	
3 <sub>h</sub>	1000	31.6	1920	

TABLE 1. Physical parameters: subscript  $h$  in the case number denotes a higher Reynolds number.

turns in the direction of the pressure gradient, forming the well-known Ekman spiral. A constant density gradient is applied as the upper boundary condition while the density gradient is set to zero at the wall. Since a large-eddy simulation is used to examine this flow, the filtered governing equations are numerically integrated in time. Using the friction velocity,  $u_*$ , the turbulent Ekman-layer depth,  $\delta = u_*/f$ , and the outer-layer density gradient,  $d\rho/dz_\infty$ , the filtered non-dimensional incompressible governing equations can be written:

$$\frac{\partial \bar{\mathbf{u}}}{\partial t} + \bar{\mathbf{u}} \cdot \nabla \bar{\mathbf{u}} = -\frac{1}{\rho_0} \nabla \bar{p}' + f \hat{\mathbf{k}} \times (U_\infty \hat{\mathbf{i}} - \bar{\mathbf{u}}) - Ri_* \frac{\bar{\rho}'}{\rho_0} \hat{\mathbf{k}} + \frac{1}{Re_*} \nabla^2 \bar{\mathbf{u}} - \nabla \cdot \boldsymbol{\tau}, \quad (2.1)$$

$$\frac{\partial \bar{\rho}'}{\partial t} + \bar{\mathbf{u}} \cdot \nabla \bar{\rho}' = \frac{1}{Re_* Pr} \nabla^2 \bar{\rho}' - \nabla \cdot \boldsymbol{\lambda}, \quad (2.2)$$

$$\nabla \cdot \bar{\mathbf{u}} = 0, \quad (2.3)$$

where

$$Re_* = \frac{u_* \delta}{\nu}, \quad Ri_* = -\frac{g}{\rho_0} \frac{d\rho}{dz_\infty} \frac{\delta^2}{u_*^2} = \frac{N_\infty^2}{f^2}, \quad Pr = \frac{\nu}{\kappa}. \quad (2.4)$$

Here,  $\rho_0$  is the constant density which has been used to apply the Boussinesq approximation,  $\nu$  is the molecular kinematic viscosity,  $\kappa$  is the molecular diffusivity,  $f$  is the Coriolis parameter,  $N_\infty$  is the free-stream buoyancy frequency, and  $\boldsymbol{\tau}$  and  $\boldsymbol{\lambda}$  are the subgrid-scale stress and density flux, respectively. The parameters considered in this study are given in table 1. Density changes are assumed to be caused by temperature variation in water, motivating the choice of Prandtl number,  $Pr = 5$ . We have performed simulations at three different values of  $Ri_*$ , equivalent to changing the free-stream temperature gradient, and at two Reynolds numbers. For the cases with  $Ri_* = 0$ , the temperature acts like a passive scalar since the temperature and momentum equations are decoupled. For comparison with oceanographic conditions, observations of the bottom boundary layer over the Oregon shelf by Perlin *et al.* (2007) provide estimates of  $Re_* = 60000$  and  $N_\infty/f = 75$ . Therefore, the Reynolds number considered in the present study is much smaller than that found in the ocean whereas the stratification levels are comparable.

The vertical domain size is  $8\delta$ , significantly larger than the boundary-layer thickness which is about  $0.5\delta$  for an unstratified turbulent Ekman layer (Coleman, Ferziger & Spalart 1990). The large vertical domain provides a region above the boundary layer where the internal wave propagation can be examined. In order to allow waves to exit freely from the top of the domain, an open boundary condition has been used with a combination of a sponge layer and a radiation condition (Klemp & Durran 1983).

The horizontal boundaries are periodic, which is consistent with the assumption that the flow is statistically homogeneous in the horizontal plane. A horizontal domain size of  $4\delta$  has been chosen to be sufficiently large that the autocorrelation in the turbulent boundary layer is small at the scale of the domain size, limiting the energy in spurious box modes.

In order to simulate this flow at larger Reynolds numbers than would otherwise be possible, a near-wall model large-eddy simulation (NWM-LES) has been used. The LES is based on a mixed model that consists of eddy viscosity and scale-similar components, and uses the dynamic procedure of Germano *et al.* (1991) to evaluate the Smagorinsky coefficient. This subgrid-scale model has been shown to perform well for stratified flow (Armenio & Sarkar 2002; Taylor, Sarkar & Armenio 2005). A near-wall model alleviates the need to resolve the viscous scales near the wall, allowing a coarser grid than would otherwise be possible. The near-wall model that is used here is similar to that developed by Schumann (1975), Grotzbach (1987), and Piomelli *et al.* (1989), but has been modified for rotating flow. It assumes that the magnitude of the horizontal velocity near the wall follows a logarithmic law which has been confirmed by the authors using direct numerical simulation (DNS). We have found that the near-wall model performs well at the Reynolds numbers given in table 1, but does not adequately capture the mean velocity profile for simulations at a very large geophysically-relevant Reynolds number on a coarse grid. Spectral collocation is used in the horizontal directions, while a second-order finite difference method on a staggered grid is used in the vertical direction. The grid that has been used for these simulations is  $96 \times 96 \times 112$  cells for a domain size of  $4\delta \times 4\delta \times 8\delta$  in the  $x$ -,  $y$ - and  $z$ -directions, respectively, and 16 grid points dedicated to the sponge region from  $8\delta - 10\delta$ . The simulations are continued for about  $tf = 30$  time units, and the time step is  $tf = 10^{-3}$ , so that the integration time is quite long, about 30 000 time steps. The integration time in buoyancy time units corresponds to  $Nt = 300$  when  $Ri_* = 100$ , and  $Nt = 950$  when  $Ri_* = 1000$ .

### 3. Summary of the boundary-layer evolution

In order to initialize each case, a simulation of an unstratified turbulent Ekman layer was conducted until the mean velocity profile reached a steady state. The three-dimensional velocity field from the unstratified simulation was then used as the initial velocity field in the stratified simulations, while the temperature field was initialized with a linear undisturbed profile. In each case, the temperature profile in the boundary layer is mixed rapidly during the initial stage, and the thickness of the boundary layer is strongly influenced by the strength of the imposed stratification. The development of the temperature gradient is shown in figure 2 where angle brackets denote an average over the horizontal plane. As the mixed layer grows in time, a pycnocline forms above the boundary layer with a mean temperature gradient up to twice the initial value. Dashed lines in figure 2 show the location where the temperature gradient is equal to the outer value, thereby illustrating the upper and lower bounds of the pycnocline.

After about  $tf = 6$  time units, each case reaches a quasi-steady state where the mean velocity profile is steady, and the mixed layer grows slowly in time. This slow growth of the temperature field is persistent even at late times. Figure 3 shows the plane averaged velocity and temperature profiles at  $tf = 20$ . Only simulations with  $Re_* = 960$  are shown, but these profiles are similar at the larger Reynolds number. The thickness of the bottom mixed layer decreases with increasing  $Ri_*$ , as the amount of energy required to mix the profile to a given height increases. The velocity profiles

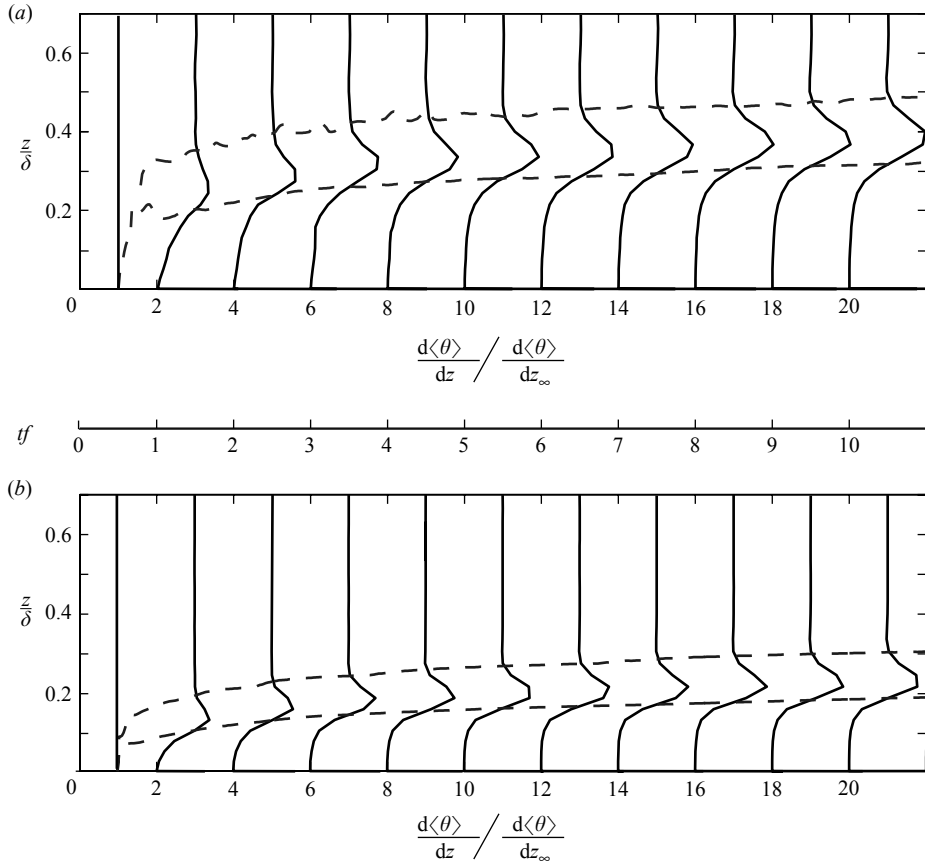


FIGURE 2. Spin-up of the plane averaged temperature gradient for  $Re_* = 960$  (a)  $Ri_* = 100$ , (b)  $Ri_* = 1000$ . Profiles of the temperature gradient are shown every  $t\tau = 1$  and offset by  $2 \times d\langle\theta\rangle/dz_\infty$ . Dashed lines show the locations where  $d\langle\theta\rangle/dz = 1$  representing the edges of the pycnocline.

are also affected by  $Ri_*$ . The mean velocity gradient in the pycnocline increases with increasing stratification and most of the Ekman transport ( $\int \langle v \rangle dz'$ ) occurs in the mixed layer. It can be shown that the Ekman transport balances the streamwise wall stress in the vertically integrated momentum equation. Therefore, if the wall stress is constant (which it is in our simulations) but the Ekman-layer depth decreases, the magnitude of  $\langle v \rangle$  should increase accordingly.

#### 4. Observations of turbulence-generated internal waves

The internal wave field generated by the boundary layer at quasi-steady state is shown through instantaneous  $x$ - $z$  slices of  $w'$  and  $\partial w'/\partial z$  in figure 4 for simulation 3. We have found that the vertical velocity field contains a significant non-propagating component in the outer layer and that  $\partial w'/\partial z$  more clearly shows the phase lines of the propagating waves which slant up and to the left. For internal waves, the group velocity,  $\mathbf{c}_g$ , is perpendicular to the wavenumber vector and parallel to the phase lines. Note that the direction of the phase lines is the same as would be seen for topographically generated waves with a flow in the positive  $x$ -direction. Figure 4(b)

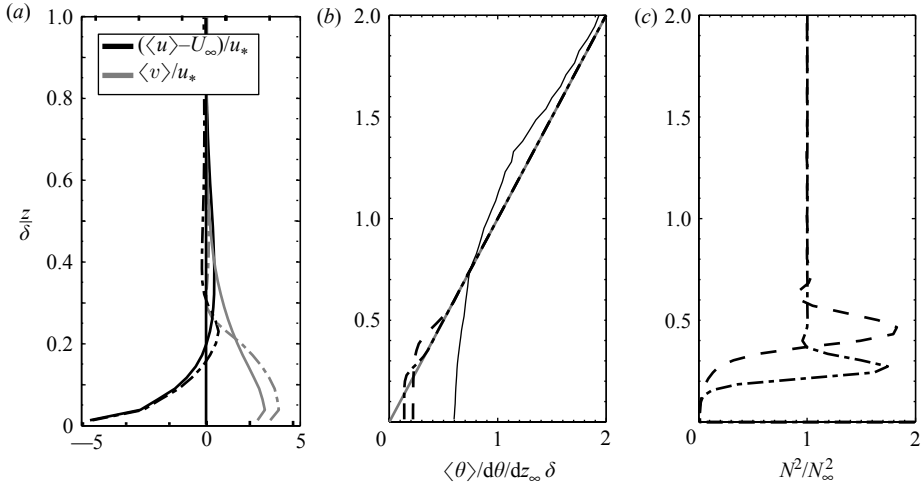


FIGURE 3. Plane averaged profiles at  $tf = 20$  and  $Re_* = 960$  (a) velocity, (b) temperature and (c) square of buoyancy frequency. For clarity, the  $Ri_* = 100$  profile is not shown in (a). The grey line in (b) shows the initial linear temperature profile. —,  $Ri_* = 0$ ; ---, 100; - · -, 1000.

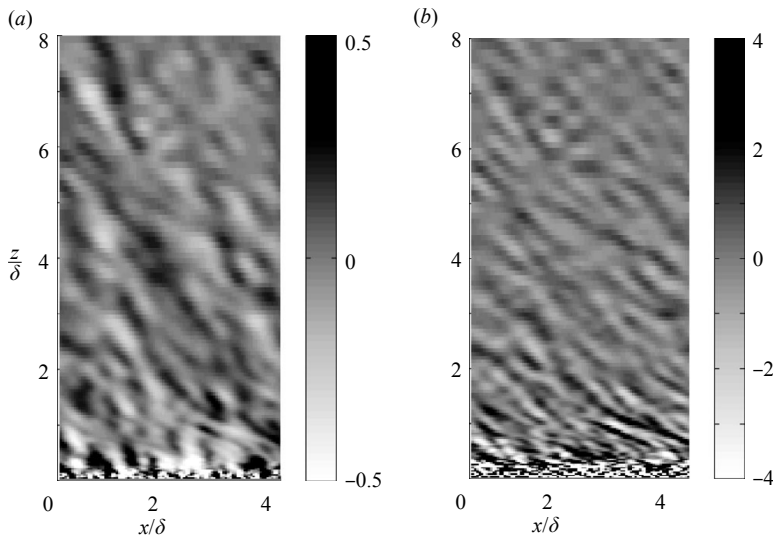


FIGURE 4. Instantaneous vertical velocity,  $Ri_* = 1000$ ,  $Re_* = 960$ ,  $tf = 20$ . At this time, the maximum temperature gradient in the pycnocline occurs at about  $0.275 \delta$ . (a)  $w'$ , (b)  $dw'/dz$ .

shows that just above the pycnocline, for  $0.5 < z/\delta < 1.5$ , there are internal waves with phase lines forming a large angle with the vertical direction. Since the dispersion relation for linear internal waves is  $\omega = N \cos \Theta$ , these waves have a lower frequency.

Since the only source of internal wave generation is the turbulent boundary layer, any waves external to the boundary layer and with a downward group velocity must be due to spurious reflections. The level of energy reflected from the upper boundary can be quantified by decomposing the spectrum into upward and downward propagating parts. This is done here by observing  $\partial w'/\partial z$  in a coordinate frame moving with  $U_\infty$  and transforming the time series for  $1 < z/\delta < 8$  into frequency and wavenumber space.

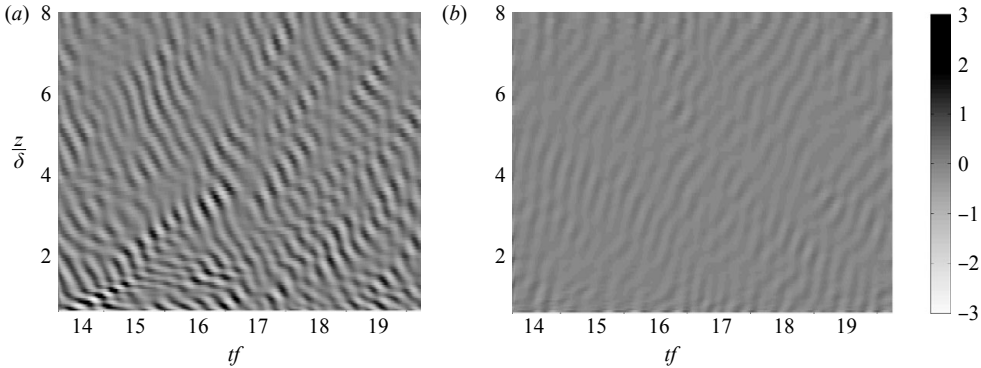


FIGURE 5. (a) Upward and (b) downward propagating wave components of  $\partial w'/\partial z$  in a frame moving with  $U_\infty$ , for  $Ri_* = 1000$  and  $Re_* = 960$ .

Since internal waves with an upward propagating group velocity are associated with downward pointing phase lines, the amplitudes in quadrants II and IV of frequency, vertical wavenumber space (with  $\omega > 0$ ,  $m < 0$ , and  $\omega < 0$ ,  $m > 0$ , respectively) are retained for the upward propagating part. An inverse Fourier transform then yields the time series in physical space for internal waves with upward energy propagation (Pinkel 2005). To obtain the reflected waves, the procedure is the same with quadrants I and III kept. The decomposition into waves with upward and downward propagating energy is shown in figure 5 for simulation 3. About 3% of the total  $(\partial w'/\partial z)^2$  field consists of downward propagating waves. A similar decomposition for the  $w'$  field (not shown) demonstrates that about 6% of the vertical kinetic energy ( $\frac{1}{2}w'^2$ ) is associated with downward energy propagation. This demonstrates that the open boundary condition used at the top of the domain performs well.

The most energetic waves observed in the pycnocline and the outer layer are qualitatively different. We can examine the contributions to the internal wave energy flux by considering the phase angle of the  $p'$ ,  $w'$  co-spectrum. With the co-spectrum,  $C_{p'w'}(k, z, t)$  and quadrature spectrum,  $Q_{p'w'}(k, z, t)$  defined as the real and imaginary parts, respectively, of

$$\sum_l \hat{w}'(k, l, z, t) \hat{p}'^*(k, l, z, t), \quad (4.1)$$

the phase angle,  $\gamma(k, z, t)$  can be defined by

$$\tan(\gamma) = \frac{Q_{p'w'}}{C_{p'w'}}. \quad (4.2)$$

Here,  $k$  and  $l$  are the wavenumbers in the  $x$  and  $y$  directions and  $*$  denotes the complex conjugate. The absolute value of the phase angle is shown for simulation 3 in figure 6. The phase angle is averaged over data at several times and linearly weighted by the absolute value of the energy at the corresponding  $k$  and  $t$ ,

$$E_{p'w'}(k, z, t) = \sum_l \hat{p}' \hat{w}'^* + \hat{p}'^* \hat{w}'. \quad (4.3)$$

The energy flux is dominated by the low wavenumbers (not shown). When  $|\gamma| = 0$ ,  $p'$  and  $w'$  are exactly in phase, while the energy flux,  $\langle p'w' \rangle$  is directed upward for  $0 \leq |\gamma| < \pi/2$  and downward for  $\pi/2 < |\gamma| \leq \pi$ . Figure 6 shows that  $|\gamma|$  is generally small in the outer layer. In the pycnocline, the most energetic modes with low

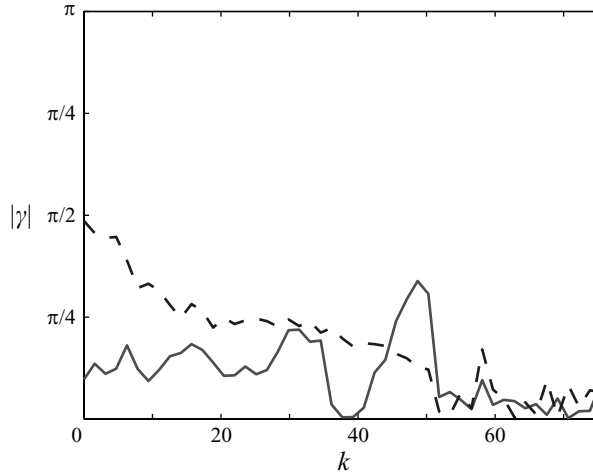


FIGURE 6. Phase angle of the  $w'$  and  $p'$  cospectrum for  $Ri_* = 1000$ ,  $Re_* = 960$ . ---,  $z/\delta = 0.3$  (pycnocline); —,  $z/\delta = 5.9$  (outer layer).

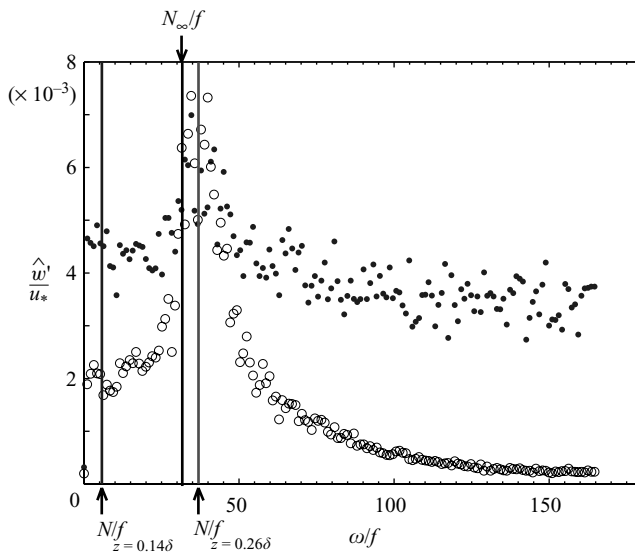


FIGURE 7. Spectral amplitudes of the vertical velocity in the pycnocline and in the boundary layer,  $Ri_* = 1000$ ,  $Re_* = 960$ . ●,  $z/\delta = 0.1438$ ; ○, 0.26.

wavenumbers have  $|\gamma| \approx \pi/2$ , so that  $p'$  and  $w'$  are about  $90^\circ$  out of phase and the vertical energy flux is small. The phase lag observed in the pycnocline is consistent with horizontally propagating interfacial waves. In laboratory experiments of a turbulent boundary layer capped by a temperature interface, Piat & Hopfinger (1981) observed a  $90^\circ$  phase lag between the vertical velocity and temperature at the interface, which is consistent with the present results if the waves are hydrostatic.

Frequency spectra obtained from the time history have been examined for dynamical coupling between different regions in the flow. Figure 7 shows the spectrum for simulation 3 at two vertical locations: at  $z/\delta = 0.14$  in the upper portion of the mixed layer where  $N/f = 5.7$ , and at  $z/\delta = 0.26$  in the pycnocline where  $N/f = 36.9$ . The

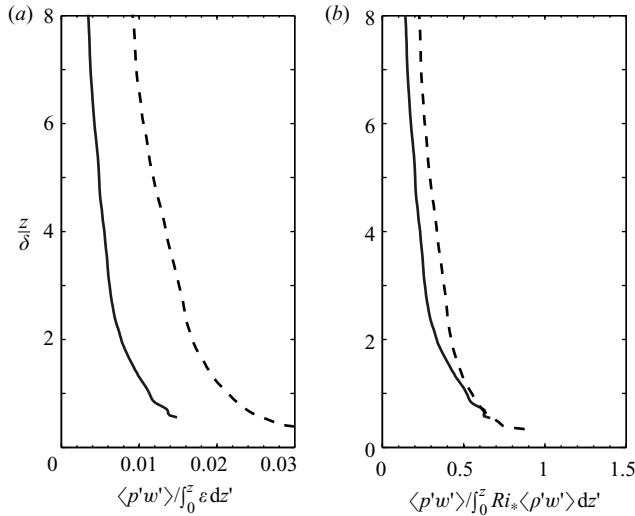


FIGURE 8. Vertical energy flux normalized by (a) the integrated dissipation, and (b) the integrated buoyancy flux with  $Re_* = 960$ . In order to ensure that assumptions made to derive (4.4) hold, the first height shown is at the top of the pycnocline where  $d\langle\rho\rangle/dz = d\rho/dz_\infty$ . —,  $Ri_* = 100$ ; ---, 1000.

spectra were obtained using a time series in a coordinate frame moving with the local mean flow and the spectral amplitudes were averaged over the horizontal plane. The energy is large over a wide range of frequencies at the lower location, signifying broadband turbulence. Both spectra have a maximum amplitude at frequencies near the buoyancy frequency in the pycnocline. At  $z/\delta = 0.14$ , this peak frequency lies outside the frequency band,  $f < \omega < N$ , for locally propagating internal waves. Since we expect nonlinear interactions between different frequencies to be strong in the turbulent boundary layer, the dynamics of turbulence in the mixed layer may be directly influenced by fluctuations in the pycnocline.

It is desirable to determine the relative importance of the radiated internal waves to the energetics of the turbulent boundary layer. We can assess this by comparing the size of the terms in the turbulent kinetic energy budget. At steady state, the turbulent kinetic energy budget integrated to a height  $z$  outside the boundary layer is:

$$\int_0^z P dz' - \int_0^z \epsilon dz' - \langle p'w' \rangle - Ri_* \int_0^z \langle w'\rho' \rangle dz' = 0, \quad (4.4)$$

where  $P$  and  $\epsilon$  are the turbulent production and dissipation, respectively, and it has been assumed that  $z$  is sufficiently large that the turbulent transport and the viscous diffusion are negligible. Here,  $\langle \cdot \rangle$  denotes an average over a horizontal plane and time, during a period when the fluctuations are quasi-steady. Figure 8(a) shows that the third term in (4.4), the vertical energy flux, is of the order of 1% of the integrated dissipation. Therefore, the energy radiated away from the boundary layer in the form of internal waves is negligible compared to the total energy extracted from the mean flow.

While the energy flux associated with radiated waves may be small compared to the integrated turbulent dissipation, the waves may still extract enough energy from the boundary layer to affect the evolution of the background potential energy. Since the kinetic energy is transferred to potential energy through the buoyancy flux, it

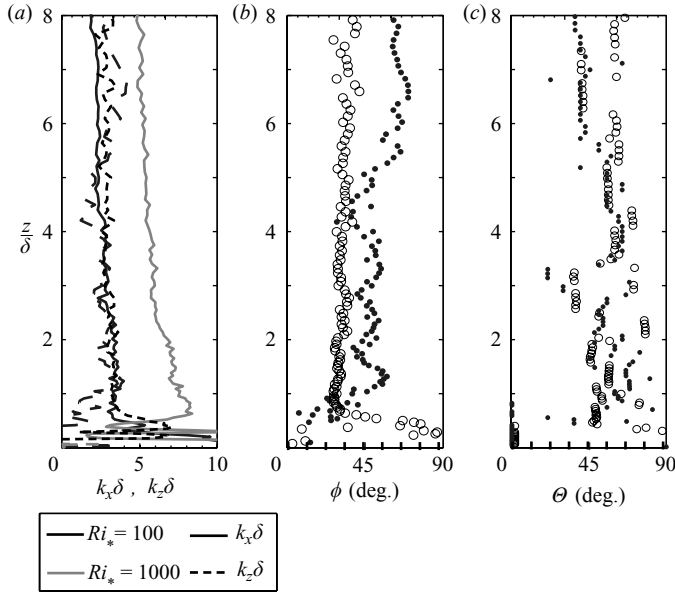


FIGURE 9. Characteristics of waves with the largest amplitude of  $\partial w'/\partial z$  for  $Re_* = 960$ . Here  $\phi$  is the azimuthal angle and  $\Theta$  is the polar angle. (b,c) ●,  $Ri_* = 100$ ; ○, 1000.

is useful to compare the internal wave energy flux to the integrated buoyancy flux (figure 8b). In both cases, the outgoing energy flux at the top of the boundary layer is of the same order and the same sign as the buoyancy flux. The integrated turbulent kinetic energy budget therefore consists of the production term balanced to within a few per cent by the dissipation. The rest of the energy extracted from the mean flow is either radiated away from the boundary layer by internal waves, or is transferred to mean potential energy.

The turbulence-generated internal waves in the simulations exhibit a characteristic propagation angle in the horizontal and vertical directions. This is illustrated for simulations 2 and 3 in figure 9. Figure 9(a) shows the horizontal wavenumbers corresponding to the maximum amplitude of  $\partial w'/\partial z$ , and figure 9(b) shows the corresponding azimuthal angle,  $\phi$  made by the wavenumber vector and the  $x$ -axis. The dominant streamwise wavenumber in the outer layer increases with stratification. Figure 9(c) shows the polar angle,  $\Theta$  made by the wavenumber vector and the horizontal plane, based on the linear dispersion relation using the dominant frequency of  $\partial w'/\partial z$ . Since the calculation of  $\Theta$  assumes that the internal waves are linear, it will be accurate only where the flow consists of small-amplitude waves, which is generally true here for  $z/\delta > 1$ . Since they are generated by a three-dimensional turbulent flow, it is remarkable that the internal waves with the largest  $\partial w'/\partial z$  are associated with a definite structure, namely azimuthal and polar angles approximately  $35^\circ - 60^\circ$  under both stratifications considered here.

We have been unable to determine any connection between the wavelength of the most dominant propagating waves and the Ozmidov scale in the boundary layer as proposed by Gibson *et al.* (2006). The Ozmidov scale (figure 10),  $L_{Oz} = \sqrt{\epsilon/N^3}$ , provides an estimate for the smallest-scale eddies that are still affected by the presence of stratification (Itsweire *et al.* 1993). In both cases,  $L_{Oz}$  is large in the turbulent mixed layer and becomes very small in the outer layer where stratification plays a dominant

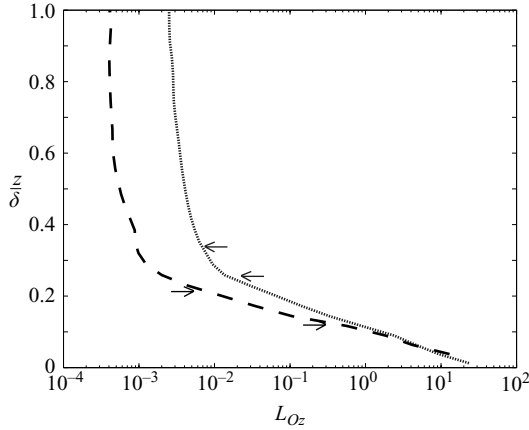


FIGURE 10. Ozmidov scale for  $Re_* = 1920$  and  $tf = 20$ . Arrows mark the region where  $\langle p'w' \rangle$  and  $d\langle p'w' \rangle/dz$  are positive. —,  $Re_* = 100$ ; ---, 1000.

role. In an attempt to estimate the region where internal waves are generated, the arrows in figure 10 mark the region where  $\langle p'w' \rangle$  and  $d\langle p'w' \rangle/dz$  are positive; that is the energy flux is upward and increasing in strength. Since  $L_{Oz}$  varies rapidly between the mixed-layer and the pycnocline, it encompasses a large range of scales in the estimated internal wave generation region. This is especially true when  $Ri_* = 1000$ , and  $L_{Oz}$  varies by more than an order of magnitude in this region. We have been unable to determine a rigorous scaling of dominant wavelength observed in the outer layer, but it appears to be set through a combination of the mixed-layer depth and the pycnocline thickness.

The stability of the internal waves can be evaluated by considering the ratio of the displacement amplitude to the horizontal wavelength. As shown by Sutherland (2001), plane waves will be unstable to density overturns if

$$\frac{A_\xi}{\lambda_x} > \frac{1}{2\pi} \cot \Theta, \quad (4.5)$$

where  $A_\xi = \Theta'/d\langle \Theta \rangle/dz$  is the approximate isopycnal displacement,  $\lambda_x$  is the horizontal wavelength, and  $\Theta$  is the angle made by the wavenumber vector and the horizontal plane. When  $\Theta$  is small, the internal wave motion is predominantly in the vertical direction, so the amplitude of the waves must become very large in order to overturn. In these cases, specifically when  $\Theta < 57.2^\circ$ , Sutherland (2001) predicts that a more restrictive criteria on the wave amplitude is based on the resonant interaction between the wave and its wave-induced mean flow. The criteria for instability due to this resonant interaction (Sutherland 2001), is

$$\frac{A_\xi}{\lambda_x} = \frac{1}{2\pi\sqrt{2}} \sin(2\Theta). \quad (4.6)$$

The ratio of the internal wave amplitude to the horizontal wavelength is shown in figure 11. Only the cases with  $Re_* = 960$  are shown here, but the result does not significantly depend on Reynolds number. The internal waves are most unstable in the pycnocline and when  $Ri_*$  is small, but in all cases, the amplitude of the internal waves is sufficiently small that they should be stable. The amplitude ratio observed here is

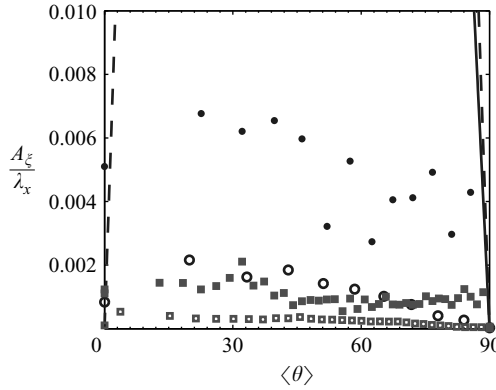


FIGURE 11. Internal wave stability estimated from the ratio of the displacement amplitude to the horizontal wavelength,  $Re_* = 960$ . For each frequency, the wavenumber corresponding to the largest slope is shown. —, OT and ---, SA show the critical amplitude ratios for overturning and self-advection instabilities, respectively. ●, simulation 2 (pycnocline); ○, simulation 2, (outer layer); ■, simulation 3 (pycnocline); □ simulation 3, (outer layer).

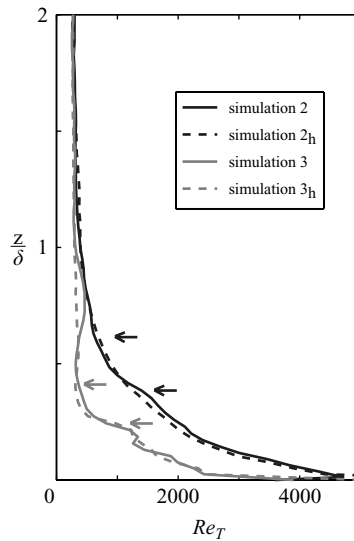


FIGURE 12. Turbulent Reynolds number. Arrows show the upper and lower bounds of the pycnocline where  $d\langle \theta \rangle / dz > 1$ .

significantly smaller than observed by Dohan & Sutherland (2003) who observed a ratio about 0.025 at  $\Theta = 45^\circ$ , which is nevertheless still predicted to be stable.

The relative sizes of the nonlinear and viscous terms can be estimated through the turbulent Reynolds number, defined as:

$$Re_T = \frac{\langle u'_i u'_i \rangle^{1/2} (2\pi/k_H)}{\nu}, \tag{4.7}$$

where  $k_H$  is the horizontal wavenumber associated with the maximum turbulent kinetic energy, and  $\langle \cdot \rangle$  denotes an average over horizontal planes and time. The turbulent Reynolds number is shown in figure 12 for simulations 2 and 3. As expected,  $Re_T$  is maximum in the turbulent boundary layer. A sharp decrease occurs in the

pycnocline (delimited by arrows in figure 12) indicating that turbulence is suppressed by the strong stratification in this region. In the outer layer, the turbulent Reynolds number approaches a relatively constant value between 200 and 300 and does not depend strongly on the Richardson number. Since we have seen in figure 9 that the dominant horizontal wavenumber in the outer layer is larger when  $Ri_* = 1000$ , the kinetic energy carried by the waves must also be larger in this case. Below the top of the pycnocline, however, the turbulent Reynolds number decreases with increasing stratification, even in the boundary-layer where the temperature gradient is negligible. It is possible that this is a result of the reduced boundary-layer thickness which limits the size of the energy-containing scales.

### 5. Viscous internal wave model

Although the generation of internal waves occurs in a region where nonlinear effects are important, the selection of a dominant range of frequencies for the internal waves propagating in the outer region can be explained by a simple linear model. It is expected that the viscous damping of internal waves should depend on the wavenumber with small-scale waves decaying more rapidly. In addition, waves with high and low frequencies are associated with a small vertical group velocity. Since they take longer to travel a given distance, they are therefore more susceptible to viscous decay. Starting with a known wave amplitude as a function of frequency and wavenumber at some initial location  $z_0$ , the wave amplitude at an arbitrary height  $z$  can be predicted based on the expected vertical propagation speed and viscous decay rate.

The linearized equations describing the evolution of a small perturbation from the background flow in a coordinate frame moving with the mean velocity can be written

$$\frac{\partial u'}{\partial t} + \langle \mathbf{u} \rangle \cdot \nabla u' + w' \frac{d \langle u \rangle}{dz} - f v' = -\frac{1}{\rho_0} \frac{\partial p'}{\partial x} + \nu \nabla^2 u', \quad (5.1)$$

$$\frac{\partial v'}{\partial t} + \langle \mathbf{u} \rangle \cdot \nabla v' + w' \frac{d \langle v \rangle}{dz} + f u' = -\frac{1}{\rho_0} \frac{\partial p'}{\partial y} + \nu \nabla^2 v', \quad (5.2)$$

$$\frac{\partial w'}{\partial t} + \langle \mathbf{u} \rangle \cdot \nabla w' = -\frac{1}{\rho_0} \frac{\partial p'}{\partial z} - \frac{\rho'}{\rho_0} g + \nu \nabla^2 w', \quad (5.3)$$

$$\frac{\partial \rho'}{\partial t} + w' \frac{d \langle \rho \rangle}{dz} = \kappa \nabla^2 \rho'. \quad (5.4)$$

Taking the dot product of  $\mathbf{u}'$  and the momentum equations, and taking the horizontal plane-average, denoted by  $\langle \cdot \rangle$ , gives

$$\begin{aligned} \frac{\partial K}{\partial t} + \langle \mathbf{u} \rangle \cdot \nabla K = & -\langle u' w' \rangle \frac{\partial \langle u \rangle}{\partial z} - \langle v' w' \rangle \frac{\partial \langle v \rangle}{\partial z} \\ & - \frac{1}{\rho_0} \nabla \cdot \langle \mathbf{u}' p' \rangle - \frac{g}{\rho_0} \langle \rho' w' \rangle + \nu \nabla^2 K - \nu \left\langle \frac{\partial u'_i}{\partial x_j} \frac{\partial u'_i}{\partial x_j} \right\rangle, \end{aligned} \quad (5.5)$$

where  $K = \langle u'_i u'_i \rangle / 2$  is the perturbation kinetic energy. Since  $K$  is only a function of  $z$  and  $t$ , and  $\langle w \rangle = 0$ , the convective term  $\langle \mathbf{u} \rangle \cdot \nabla K = 0$ . When (5.5) is taken to apply away from the boundary layer where  $\partial \langle u \rangle / \partial z \approx 0$  and  $\partial \langle v \rangle / \partial z \approx 0$ , it simplifies to

$$\frac{\partial K}{\partial t} = -\frac{1}{\rho_0} \nabla \cdot \langle \mathbf{u}' p' \rangle - \frac{g}{\rho_0} \langle \rho' w' \rangle + \nu \frac{\partial^2 K}{\partial z^2} - \nu \left\langle \frac{\partial u'_i}{\partial x_j} \frac{\partial u'_i}{\partial x_j} \right\rangle. \quad (5.6)$$

Similarly, multiplying (5.4) by  $\rho'$  and taking the plane average gives

$$\frac{\partial P}{\partial t} = \frac{g}{\rho_0} \langle \rho' w' \rangle + \kappa \frac{\partial^2 P}{\partial z^2} + \frac{g}{\rho_0 \partial \langle \rho \rangle / \partial z} \kappa \left\langle \frac{\partial \rho'}{\partial x_j} \frac{\partial \rho'}{\partial x_j} \right\rangle, \quad (5.7)$$

where the perturbation potential energy is defined by

$$P = \frac{-g \langle \rho'^2 \rangle}{2\rho_0 (d \langle \rho \rangle / dz)}. \quad (5.8)$$

Using the general form for a plane wave,  $u'_i = \hat{u}_i \exp[i(\mathbf{k} \cdot \mathbf{x} - \omega t)]$ , the kinetic and potential energy dissipation can be written as

$$\epsilon = -\nu \left\langle \frac{\partial u'_i}{\partial x_j} \frac{\partial u'_i}{\partial x_j} \right\rangle = -\nu |\mathbf{k}|^2 \langle u'_i u'_i \rangle, \quad (5.9)$$

$$\epsilon_\rho = -\kappa \left\langle \frac{\partial \rho'}{\partial x_j} \frac{\partial \rho'}{\partial x_j} \right\rangle = -\kappa |\mathbf{k}|^2 \langle \rho' \rho' \rangle. \quad (5.10)$$

An equation for the wave energy,  $W = \rho_0 (P + K)$  can be found by summing (5.6) and (5.7). If  $Pr = 1$ , the wave energy then satisfies

$$\frac{\partial W}{\partial t} + \nabla \cdot (W \mathbf{c}_g) = \nu \frac{\partial^2 W}{\partial z^2} - 2\nu |\mathbf{k}|^2 W, \quad (5.11)$$

where we have used the result that the energy flux  $\langle p' \mathbf{u}' \rangle = \mathbf{c}_g W$  where  $\mathbf{c}_g$  denotes the group velocity vector. If we make the approximation that the mean wave energy and the background stratification vary slowly in  $z$ , then viscous dissipation dominates the diffusion term, and the previous equation can be rewritten as

$$\frac{DW}{Dt} = -2\nu |\mathbf{k}|^2 W - W \nabla \cdot \mathbf{c}_g, \quad (5.12)$$

where  $D/Dt$  denotes a derivative following the group velocity of the wave. For waves in a slowly varying medium,  $\nabla \cdot \mathbf{c}_g \approx 0$  so that with this approximation

$$\frac{DW}{Dt} = -2\nu |\mathbf{k}|^2 W. \quad (5.13)$$

For convenience, we can recast (5.13) in terms of the vertical velocity. For a plane wave with an unknown  $z$ -dependence, the vertical velocity can be expressed as

$$w = A(z, t) \exp[i(kx + ly - \omega t + \theta(z))]. \quad (5.14)$$

By inserting equations of this form into (5.1)–(5.4), the wave energy can be expressed in terms of the vertical velocity amplitude

$$W = \frac{1}{2} \rho_0 A^2 \frac{|\mathbf{k}|^2}{k_h^2}. \quad (5.15)$$

Again, assuming that the background density gradient and the wave amplitude vary on scales larger than the wavelength, and since  $k_h$  and  $\omega$  are constant following internal wave rays (Pedlosky 2003), (5.13) simplifies to

$$\frac{D}{Dt} (|\mathbf{k}|^2 A^2) = -2\nu |\mathbf{k}|^4 A^2. \quad (5.16)$$

In a coordinate frame moving with the group velocity, (5.16) can be integrated to give

$$A^2(z, t) = A_0^2 \frac{|\mathbf{k}_0|^2}{|\mathbf{k}|^2} \exp \left( \int_0^t -2\nu |\mathbf{k}|^2 dt \right), \quad (5.17)$$

or

$$A(z, t) = A_0 \frac{|\mathbf{k}_0|}{|\mathbf{k}|} \exp \left( \int_0^t -\nu |\mathbf{k}|^2 dt \right). \quad (5.18)$$

We can obtain an expression for the expected vertical velocity amplitude as a function of  $z$  in a stationary reference frame by using the vertical component of the group velocity for a rotating internal wave (Pedlosky 2003)

$$c_{gz} = \frac{\partial \omega}{\partial m} = -\frac{m}{\omega} \frac{\omega^2 - f^2}{|\mathbf{k}|^2} = \frac{k_h}{\omega |\mathbf{k}|^2} (\omega^2 - f^2)^{1/2} (N^2 - \omega^2)^{1/2} = \frac{dz}{dt}, \quad (5.19)$$

which makes use of the dispersion relation for internal waves with rotation

$$m = -k_H \left[ \frac{N^2 - \omega^2}{\omega^2 - f^2} \right]^{1/2}. \quad (5.20)$$

The negative branch of  $m$  has been chosen since we are interested in waves with an energy flux directed upward. The expected amplitude for a given frequency and horizontal wavenumber, expressed as a function of  $z$  in an Eulerian frame is then

$$A(z) = A_0 \frac{|\mathbf{k}_0|}{|\mathbf{k}|} \exp \left[ \frac{-\nu \omega}{k_h} (\omega^2 - f^2)^{-1/2} \int_{z_0}^z |\mathbf{k}|^4 (N^2 - \omega^2)^{-1/2} dz' \right]. \quad (5.21)$$

From (5.19), it is clear that for low- and high-frequency waves ( $\omega = f$  and  $\omega = N(z)$ , respectively) the vertical component of the group velocity vanishes. It also follows from (5.21) that when the frequency is near these limits, the wave amplitude decays rapidly as a function of  $z$ . For a fixed horizontal wavenumber, it can be shown that the vertical component of the group velocity is maximum for waves with  $\omega^2 = (2/3)N^2$ , which propagate at  $\theta = 35^\circ$ . (Note that when the magnitude of the wavenumber vector,  $|\mathbf{k}|$  is held constant, the group velocity maximum is at  $\theta = 45^\circ$ , see Gill 1982) It is of interest to find the frequency that is associated with the smallest rate of viscous decay. For a fixed horizontal wavenumber and a constant background stratification, the minimum rate of decay, determined from (5.21), occurs at  $\omega = \sqrt{4/5}N$ , or  $\theta = 26.6^\circ$ . Note that while waves at this frequency are expected to decay the slowest, the amplitude at a given height is strongly dependent on the distribution of the initial wave amplitude  $A_0(k_h, \omega)$ .

The proposed model for the propagation of internal waves then proceeds as follows. Start with an initial estimate for the internal wave amplitude  $A_0(k_H, \omega)$  at a height  $z_0$ . Then use the expression for  $m(z)$  given by (5.20) for a given  $N(z)$  profile, to numerically integrate (5.21) for every value of  $k_H$  and  $\omega$ . The performance of the viscous internal wave model has been evaluated by using the observed internal wave spectrum from the simulations at the bottom of the pycnocline. The location  $z_0$  is chosen in each case by using two conditions. First,  $z_0$  should be above the height where  $\langle p'w' \rangle$  is maximum, with the expectation that most of the waves have been generated below this level. In addition,  $z_0$  should be chosen so that  $N(z_0) \geq N_\infty$  to ensure that all frequencies  $f < \omega < N_\infty$  correspond to vertically propagating waves.

The viscosity that appears in (5.21) is taken to be the molecular value. In our simulations, since the perturbation amplitude in the outer layer is small, the eddy viscosity in this region is zero, so this is the proper choice. In a situation where an

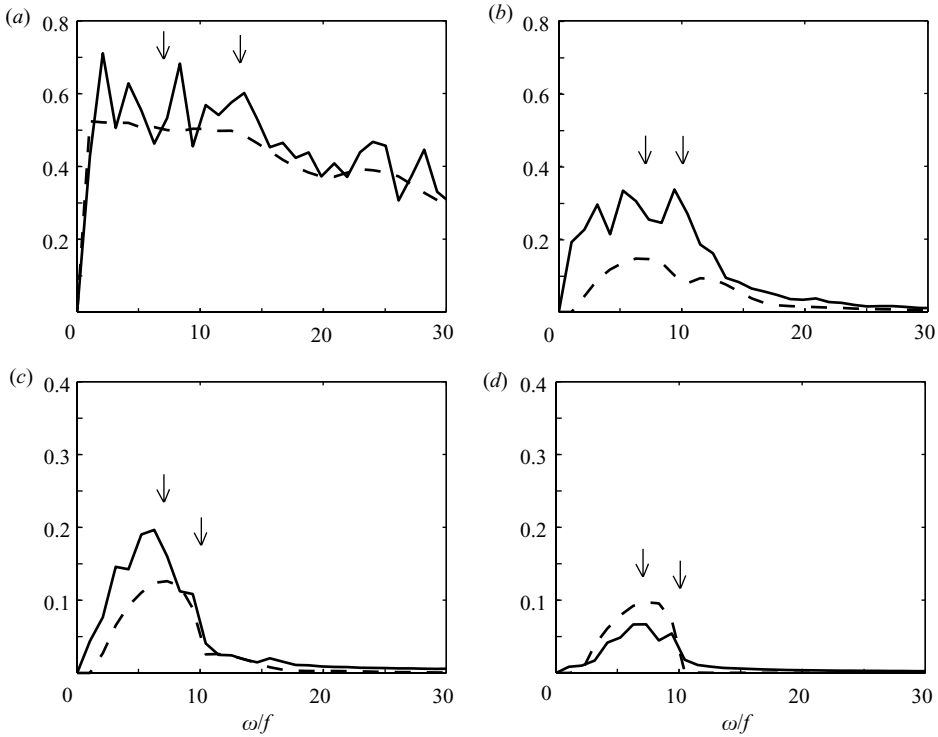


FIGURE 13. Comparison between observed (solid line) and predicted (dashed line) spectra of  $\partial w'/\partial z$  using a viscous internal wave model for  $Ri_* = 100$ ,  $Re_* = 960$ . Arrows show  $N_\infty/(\sqrt{2}f)$  (left) and  $N(z)/f$  (right). Note that (a,b) and (c,d) have different y-axis scales. (a)  $z/\delta = 0.45$ ; (b) 1; (c) 2; (d) 8.

eddy viscosity is present in the outer layer, it would be possible to re-derive (5.21) with  $\nu_T(z)$ . We have derived the model equations with a Prandtl number of unity, but altering the viscosity in (5.21) by a small fraction does not qualitatively affect the results. It is important to note that this model is linear and neglects the turbulent production and assumes that the background flow is slowly varying.

In order to estimate  $A_0(k_H, \omega)$ , the frequency/wavenumber spectrum for  $\partial w'/\partial z$  in a reference frame moving with the plane-averaged horizontal velocity is divided by  $m(z_0)$  as estimated from (5.20). This effectively filters out the high-frequency waves in the pycnocline that do not propagate vertically. The spectral amplitudes are then smoothed in frequency space to obtain  $A_0(k_H, \omega)$  used in (5.21). Frequencies with  $\omega > N(z)$  are allowed to decay exponentially in the vertical direction, representing evanescent modes with  $A = A_0 \exp[im(z - z_0)]$  where  $m$ , calculated using (5.20), is imaginary.

The estimate of the spectrum of  $\partial w'/\partial z$  from the viscous decay model is compared with the corresponding spectrum from the simulations in figures 13 and 14. In order to show the combined contributions of all values of  $k_H$ , the square root of the sum of the squared amplitudes of  $\partial w'/\partial z$  are shown as a function of  $\omega/f$  in these figures. The initial spectrum at  $z_0$ , shown in figures 13(a) and 14(a), peaks at low frequencies. Arrows indicate the local values of  $N/f$  and  $N_\infty/(\sqrt{2}f)$ . As they propagate vertically, the waves with large and small frequencies decay, leaving a central peak. Generally, the viscous internal wave model predicts the decay of the wave magnitude well.

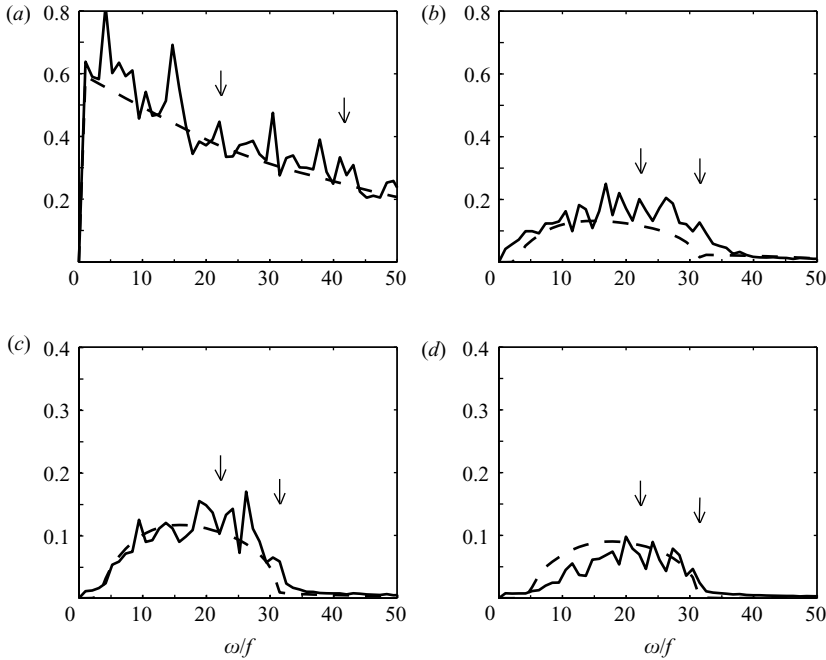


FIGURE 14. As figure 13 but for  $Ri_* = 1000$ ,  $Re_* = 960$ . (a)  $z/\delta = 0.26$ ; (b) 1; (c) 2; (d) 8.

However, the model tends to overestimate the decay rate for  $z < \delta$ , especially for the low stratification case. This may be due to a combination of the neglect of the turbulent production, the presence of non-propagating modes, and a breakdown of the WKB assumption of a slowly varying background state. Nevertheless, in the outer layer, the shape of the spectrum and the frequency associated with the largest amplitude are generally captured by this simple model, both for moderate ( $Ri_* = 100$ ) and large ( $Ri_* = 1000$ ) stratification.

The dependence of the viscous internal wave model on the Reynolds number is examined in figure 15 for  $Ri_* = 1000$ . Here, the spectra at  $z_0$  are assumed to be independent of Reynolds number. This assumption is made in order to proceed to high-Reynolds-numbers beyond the available simulation data. Comparison of the data at  $Re_* = 960$  and  $Re_* = 1920$  shows that the turbulence spectra for  $\omega < N$  are not significantly different, but future simulations of high-Reynolds-number boundary layers are necessary to obtain the appropriate Reynolds-number scaling. The model prediction using the molecular viscosity corresponding to both Reynolds numbers considered here are shown, together with a much larger Reynolds number,  $Re_* = 60\,000$ , that would be typical of oceanic conditions. Even at the large Reynolds number, the viscous model predicts that the high and low frequencies decay sufficiently to create a central spectral peak. It is possible that nonlinear effects could become important at a large Reynolds number, or that the generated wave spectrum could change. Simulations or experiments at a larger Reynolds number should be carried out in the future to test the viscous decay mechanism in this situation.

It is of interest to determine the influence of the initial amplitude distribution,  $A_0(k_h, \omega)$ , on the model results. Figure 16 compares the model predictions when  $A_0$  is taken from the LES data to a case where the initial amplitude is independent of  $k_h$  and  $\omega$ . In order to isolate the influence of the initial amplitude and to compare to the

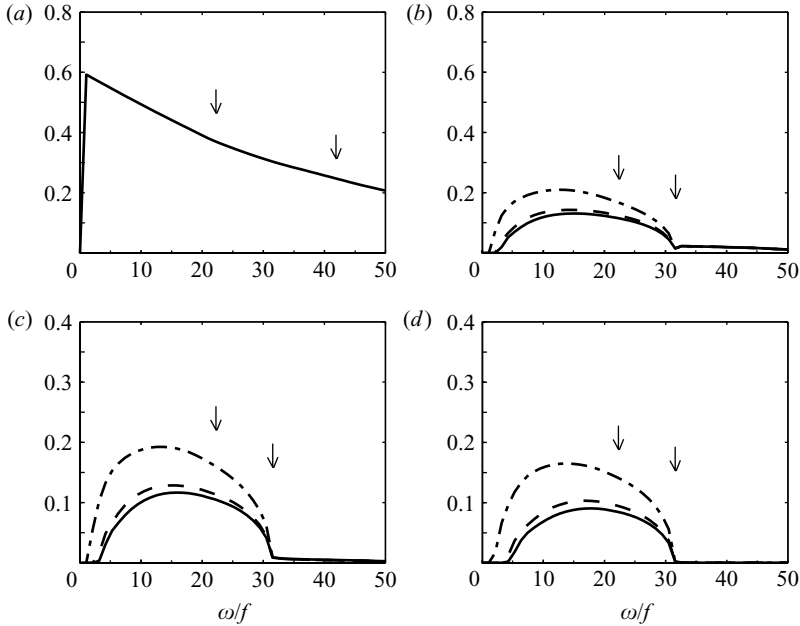


FIGURE 15. Predicted spectrum of  $\partial w'/\partial z$  for  $Ri_* = 1000$  and various Reynolds numbers: —,  $Re_* = 960$ ; ---,  $Re_* = 1920$ ; -·-,  $Re_* = 60000$ . Arrows show  $N_\infty/(\sqrt{2}f)$  (left) and  $N(z)/f$  (right). Note that (a,b) and (c,d) have different y-axis scales. (a)  $z/\delta = 0.26$ ; (b) 1; (c) 2; (d) 8.

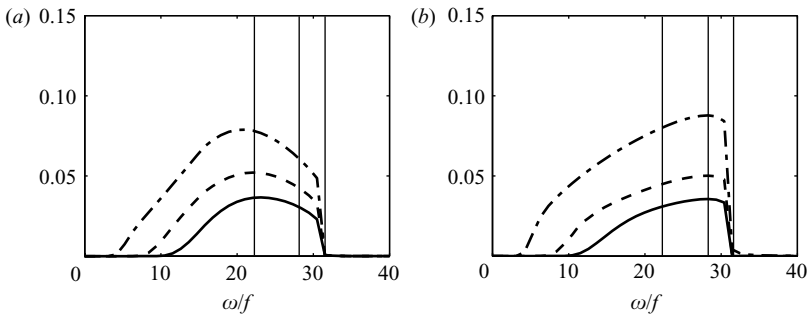


FIGURE 16. Predicted spectrum of  $\partial w'/\partial z$  for  $Ri_* = 1000$  at various heights for (a) Initial amplitude distribution  $A_0(k_h, \omega)$  taken from simulation data and (b) uniform initial amplitude,  $A_0$  independent of  $\omega$  and  $k_h$ . In both cases, the initial height  $z_0 = 2\delta$ . Vertical lines show  $N_\infty/(\sqrt{2}f)$  (left),  $\sqrt{4/5}N_\infty/f$  (centre) and  $N_\infty/f$  (right). -·-,  $z/\delta = 8$ ; ---, 100; —, 400.

predicted decay in a uniform background flow, the initial height is set to  $z_0 = 2\delta$ . At this location, the mean density gradient is equal to the free-stream value. Figure 16(b) shows that when starting from a uniform initial amplitude (with  $A_0$  independent of  $k_h$  and  $\omega$ ) the maximum amplitude of the propagating waves occurs at  $\omega = \sqrt{4/5}N$ . It can be shown analytically that this frequency corresponds to the minimum rate of decay as predicted by the viscous decay model. When using the simulation data to set  $A_0(k_h, \omega)$  as shown in figure 16(a), the frequency associated with the maximum wave amplitude increases with  $z$ , but does so very slowly. Even at a height of  $z/\delta = 400$ , the maximum wave amplitude occurs at a frequency less than  $\sqrt{4/5}N$ . If  $\delta = u_* / f = 25$  m, as roughly estimated from the data of Perlin *et al.* (2007), then  $z = 400\delta = 10$  km.

This implies that the initial amplitude distribution set up by the turbulent generation process may affect the distribution of wave amplitudes far from the source.

## 6. Discussion of the internal wave model

While a differential viscous decay explains the amplitude and spectral shape of the turbulence-generated internal waves observed in our simulations, it remains to be determined whether this mechanism can explain the results of other experiments, particularly in those cases with larger amplitude waves. This should be possible to test, particularly from other numerical simulations. The observed amplitude of  $w'$  as a function of  $\omega$  and  $k_H$  just beyond the wave-generation site can be used in (5.21) to obtain the predicted amplitude  $A(\omega, k_H, z)$  which can then be compared to the observed wave field.

The differential viscous decay mechanism was considered by Dohan & Sutherland (2005). They rejected this explanation partly because they expected that it would yield waves at the frequency associated with the maximum vertical group velocity,  $\Theta \approx 35^\circ$ , while they observed  $\Theta \approx 45^\circ$ . As we have shown, differential viscous decay is able to produce waves near  $45^\circ$  since the distribution of initial wave amplitudes is shifted towards low frequencies and therefore larger angles of vertical propagation and since  $\omega$  depends on  $|\mathbf{k}|$  through the dispersion relation. Sutherland & Linden (1998) hypothesized that the narrow frequency band that they observed for turbulence-generated internal waves was due to nonlinear interactions between the waves and turbulence. Since we have seen that the local Reynolds number in the region of internal wave production is large, this mechanism cannot be ruled out and warrants further investigation. However, as we have shown, a simpler mechanism of viscous decay is capable of capturing many of the features of the observed frequency spectrum.

## 7. Conclusions

We have conducted simulations of a turbulent Ekman layer over a flat wall. A uniform stratification was applied initially and maintained as the upper boundary condition, and the temperature gradient was set to zero at the lower wall. As the flow developed, a well-mixed turbulent region formed near the wall, capped by a strongly stratified pycnocline. It has been established that turbulence in a bottom Ekman layer, when subject to an overlying stratification, radiates internal waves. The primary focus of this paper was an analysis of this internal wave field. It is worth noting that the internal waves are radiated by turbulence in a well-mixed region in this problem, in contrast to the stratified turbulence that is often seen in wakes and shear layers.

Two types of internal waves were observed in the simulations. The first type of waves have frequencies larger than the outer-layer buoyancy frequency and were observed in the pycnocline. The pressure perturbation and the vertical velocity of these waves were nearly  $90^\circ$  out of phase, indicating horizontally propagating waves associated with a small vertical energy flux. Above the boundary layer, these waves decayed as evanescent modes since their frequency is not between  $f$  and  $N$ . In the boundary layer, the turbulent spectrum exhibited a peak at the same frequency as observed for waves in the pycnocline, which indicates the potential for nonlinear interactions between the boundary-layer turbulence and the pycnocline waves. Since regions of strong density gradient are commonly observed above turbulent boundary layers in both the ocean and atmosphere, investigating the influence of the pycnocline

waves on the boundary-layer turbulence would be an important topic for further study.

The second type of waves that were observed here are associated with frequencies  $f < \omega < N_\infty$  and therefore able to propagate in the outer layer. Considering that they were excited from a turbulent region with a broad range of frequencies and scales, it is remarkable that these waves were associated with a distinct peak in frequency and wavenumber space. The vertical angle of propagation was between  $35^\circ$  and  $60^\circ$ , which is consistent with several previous studies of turbulence-generated internal waves. As we have shown, the decay in amplitude and the formation of a spectral peak is consistent with a linear viscous decay. Although the mechanism that we have proposed to explain the propagation angle observed for waves propagating in the outer layer relies on the effects of molecular viscosity, our model indicates that the formation of a distinct spectral peak is possible even at a realistically large oceanic Reynolds number.

It can be shown that the viscous model presented here predicts that waves propagating at  $\Theta = 26.6^\circ$  have the slowest rate of decay. Nevertheless, when starting with initial wave amplitudes weighted towards low frequencies as observed in the simulations, the observed and predicted waves show a maximum amplitude at larger angles. Using the model prediction, we have shown that the initial distribution of wave amplitudes affects the wave field at very large distances away from the boundary layer. This implies that knowledge of the boundary-layer turbulence is important for predicting the amplitude and spectral content of turbulence-generated internal waves far from the generation site.

The importance of the internal wave energy flux to the boundary-layer energetics has been estimated by comparing the magnitudes of the terms in the vertically integrated turbulent kinetic energy equation. It was found that the dominant balance is between production and dissipation in the boundary layer and that the vertical energy flux is only a few per cent of these terms. However, most of the production and dissipation occurs in the mixed region where stratification effects are not directly felt. We have found that the internal wave energy flux and the integrated buoyancy flux are the same order in the pycnocline. Since the buoyancy flux is a measure of the energy transferred from kinetic to potential, if all of the energy radiated away from the boundary layer as internal waves were instead present as an additional buoyancy flux, the evolution of the local mean temperature profile in the pycnocline would be significantly affected.

The support of grant N00014-05-1-0334 from ONR Physical Oceanography, program manager Dr Scott Harper, is gratefully acknowledged.

#### REFERENCES

- AGUILAR, D. A. & SUTHERLAND, B. R. 2006 Internal wave generation from rough topography. *Phys. Fluids* **18** (066603), 1–9.
- ARMENIO, V. & SARKAR, S. 2002 An investigation of stably stratified turbulent channel flow using large-eddy simulation. *J. Fluid Mech.* **459**, 1–42.
- BASAK, S. & SARKAR, S. 2006 Dynamics of a stratified shear layer with horizontal shear. *J. Fluid Mech.* **568**, 19–54.
- BONNETON, P., CHOMAZ, J. M. & HOPFINGER, E. J. 1993 Internal waves produced by the turbulent wake of a sphere moving horizontally in a stratified fluid. *J. Fluid Mech.* **254**, 23–40.
- BUHLER, O. & MCINTYRE, M. E. 1999 On shear-generated gravity waves that reach the mesosphere. Part II: Wave propagation. *J. Atmos. Sci.* **56**, 3764–3773.

- BUHLER, O., MCINTYRE, M. E. & SCINOCCA, J. F. 1999 On shear-generated gravity waves that reach the mesosphere. Part I: Wave generation. *J. Atmos. Sci.* **56**, 3749–3763.
- COLEMAN, G. N., FERZIGER, J. H. & SPALART, P. R. 1990 A numerical study of the turbulent Ekman layer. *J. Fluid Mech.* **213**, 313–348.
- D'ASARO, E. 1982 Absorption of internal waves by the benthic boundary layer. *J. Phys. Oceanogr.* **12**, 323–336.
- DIAMESSIS, P. J., DOMARADZKI, J. A. & HESTHAVEN, J. S. 2005 A spectral multidomain penalty method model for the simulation of high Reynolds number localized incompressible stratified turbulence. *J. Comput. Phys.* **202** (1), 298–322.
- DOHAN, K. & SUTHERLAND, B. R. 2003 Internal waves generated from a turbulent mixed region. *Phys. Fluids* **15** (2), 488–498.
- DOHAN, K. & SUTHERLAND, B. R. 2005 Numerical and laboratory generation of internal waves from turbulence. *Dyn. Atmos. Oceans* **40**, 43–56.
- E, X. & HOPFINGER, E. J. 1986 On mixing across an interface in stably stratified fluid. *J. Fluid Mech.* **166**, 227–244.
- FLYNN, M. R. & SUTHERLAND, B. R. 2004 Intrusive gravity currents and internal gravity wave generation in stratified fluid. *J. Fluid Mech.* **514**, 355–383.
- FRITTS, D. C. & ALEXANDER, M. J. 2003 Gravity wave dynamics and effects in the middle atmosphere. *Rev. Geophys.* **41** (1003), doi:10.1029/2001RG000106.
- GARRETT, C. & ST LAURENT, L. 2002 Aspects of deep ocean mixing. *J. Oceanogr.* **58**, 11–24.
- GERMANO, M., PIOMELLI, U., MOIN, P. & CABOT, W. H. 1991 A dynamic subgrid-scale eddy viscosity model. *Phys. Fluids A* **3** (7), 1760–1765.
- GIBSON, C. H., BONDUR, V. G., KEELER, R. N. & LEUNG, P. T. 2006 Energetics of the beamed zombie turbulence maser action mechanism for remote detection of submerged oceanic turbulence. *J. Appl. Fluid Mech.* **1** (1), 11–42.
- GILL, A. E. 1982 *Atmosphere–Ocean Dynamics*. Academic.
- GOURLAY, M. J., ARENDT, S. C., FRITTS, D. C. & WERNE, J. 2001 Numerical modeling of initially turbulent wakes with net momentum. *Phys. Fluids* **13** (12), 3783–3802.
- GREGG, M. C., WINKEL, D. W., MACKINNON, J. A. & LIEN, R. C. 1999 Mixing over shelves and slopes. In *Dynamics of Oceanic Internal Gravity Waves II, Proceedings, Hawaiian Winter Workshop* (ed. P. Muller & D. Henderson), pp. 37–45.
- GROTZBACH, G. 1987 Direct numerical and large eddy simulation of turbulent channel flows. In *Encyclopedia of Fluid Mechanics* (ed. N. P. Chermisinoff), vol. 6, pp. 1337–1391. Gulf, West Orange, NJ.
- HOLTON, J. R. & ALEXANDER, M. J. 2000 The role of waves in the transport circulation of the middle atmosphere. In *AGU Monograph: Science Across the Stratopause*, pp. 21–35. American Geophysical Union.
- ITSWEIRE, E. C., KOSEFF, J. R., BRIGGS, D. A. & FERZIGER, J. H. 1993 Turbulence in stratified shear flows: implications for interpreting shear-induced mixing in the ocean. *J. Phys. Oceanogr.* **23**, 1508–1522.
- KEELER, R. N., BONDUR, V. G. & GIBSON, C. H. 2005 Optical satellite imagery detection of internal wave effects from a submerged turbulent outfall in a stratified ocean. *Geophys. Res. Lett.* **32** (L12610), 1–5.
- KLEMP, J. B. & DURRAN, D. R. 1983 An upper boundary condition permitting internal gravity wave radiation in numerical mesoscale models. *Mon. Weather Rev.* **111**, 430–444.
- LINDEN, P. F. 1975 The deepening of a mixed layer in a stratified fluid. *J. Fluid Mech.* **71**, 385–405.
- MOUM, J. N., HERBERT, D., PAULSON, C. A. & CALDWELL, D. R. 1992 Turbulence and internal waves at the equator. Part I: Statistics from towed thermistors and a microstructure profiler. *J. Phys. Oceanogr.* **22**, 1330–1345.
- PEDLOSKY, J. 2003 *Waves in The Ocean and Atmosphere: Introduction to Wave Dynamics*, 1st edn. Springer.
- PERLIN, A., MOUM, J. N., KLYMAK, J. M., LEVINE, M. D., BOYD, T. J. & KOSRO, P. M. 2007 Organization of stratification, turbulence, and veering in bottom Ekman layers. *J. Geophys. Res.* **112**, C05S90, 1–12.
- PIAT, J.-F. & HOPFINGER, E. J. 1981 A boundary layer topped by a density interface. *J. Fluid Mech.* **113**, 411–432.

- PINKEL, R. 2005 Near-inertial wave propagation in the western Arctic. *J. Phys. Oceanogr.* **35** (5), 645–665.
- PIOMELLI, U., FERZIGER, J., MOIN, P. & KIM, J. 1989 New approximate boundary conditions for large eddy simulations of wall-bounded flows. *Phys. Fluids A* **1** (6), 1061–1068.
- SCHUMANN, U. 1975 Subgrid scale model for finite difference simulations of turbulent flows in plane channels and annuli. *J. Comput. Phys.* **18**, 376–404.
- SLINN, D. N. & RILEY, J. J. 1998 Turbulent dynamics of a critically reflecting internal gravity wave. *Theor. Comput. Fluid Dyn.* **11**, 281–303.
- SPEDDING, G. R. 2002 Vertical structure in stratified wakes with high initial Froude number. *J. Fluid Mech.* **454**, 71–112.
- SUTHERLAND, B. R. 2001 Finite-amplitude internal wavepacket dispersion and breaking. *J. Fluid Mech.* **429**, 343–380.
- SUTHERLAND, B. R. & LINDEN, P. F. 1998 Internal wave excitation from stratified flow over a thin barrier. *J. Fluid Mech.* **377**, 223–252.
- SUTHERLAND, B. R., CAULFIELD, C. P. & PELTIER, W. R. 1994 Internal gravity wave generation and hydrodynamic instability. *J. Atmos. Sci.* **51**, 3261–3280.
- TAYLOR, J. R., SARKAR, S. & ARMENIO, V. 2005 Large eddy simulation of stably stratified open channel flow. *J. Fluid Mech.* **17**, 1–18.
- THORPE, S. A. 2001 Internal wave reflection and scatter from sloping rough topography. *J. Phys. Oceanogr.* **31**, 537–553.